

RDM: Recurrent Diffusion Model for Human Motion Generation

Mirgahney Mohamed Harry Jake Cunningham Marc P. Deisenroth
 Lourdes Agapito
 Department of Computer Science, University College London

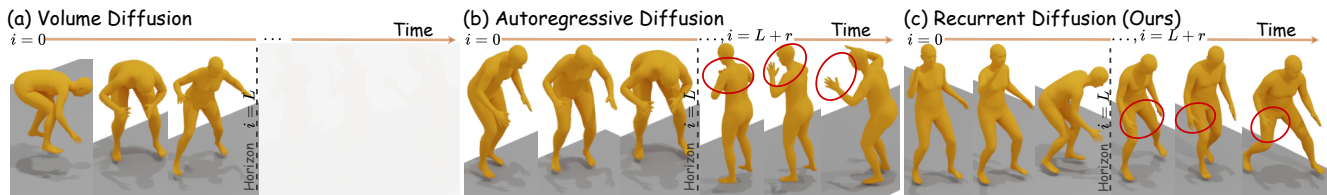


Figure 1. **Temporal diffusion generation.** Volume diffusion (a) generates sequences limited by horizon (L), shown by the dashed line; On the other hand, both autoregressive (b) and recurrent diffusion (c) extend sequences beyond the horizon ($L + r$). However, recurrent diffusion produces better-aligned sequences (see red circles) with the prompt “dribbling with a basketball”.

Abstract

Human motion generation is a challenging task due to its high dimensionality and the difficulty of generating fine-grained motions. Diffusion methods have been proposed due to their high sample quality and expressiveness. Early approaches treat the entire sequence as a whole, which is computationally expensive and restricts sequence length. In contrast, autoregressive diffusion models generate longer sequences. However, their reliance on fully denoising previous frames complicates training and inference. Consequently, we propose RDM, a new recurrent diffusion formulation similar to Recurrent Neural Networks (RNNs). RDMs explicitly condition diffusion processes on preceding noisy frames, avoiding the cost of full denoising. Nonetheless, maintaining its probabilistic nature is non-trivial. Therefore, we employ Normalizing Flows to model recurrent connections. Our evaluations demonstrate RDM’s effectiveness: it achieves comparable performance to autoregressive baselines and generates long sequences that remain aligned with the text. RDM also skips diffusion steps during inference, significantly reducing computational cost.

1. Introduction

Human motion generation is crucial in computer animation, with applications spanning gaming to robotics. Despite notable progress, it remains challenging due to the vast pos-

sible motions and sophisticated equipment required to acquire the data. Therefore, automating motion generation from natural signals, such as text, offers an intuitive interface for users and significantly reduces the effort involved.

Variational Auto-Encoders (VAEs) [25] demonstrated success in mapping various modalities to motion [28, 34, 44, 47]. Nevertheless, VAEs inherently impose restrictions on the target distribution, limiting their expressiveness.

In contrast, diffusion models [42] do not impose restrictions on target distributions [45] and exhibit excellent capacity for many-to-many distribution matching [18]. MotionDiffuse [54] and MDM [45] are pioneering works that employ diffusion methods [42] for human motion generation. MLD [5] achieves efficient training and inference by using diffusion in latent space.

However, these approaches [5, 45, 54], which we term “volume diffusion”, treat the entire sequence as a monolithic input (Fig. 2 (a)). Consequently, it contributes to motion incoherence and limits sequence generation to short, fixed horizons, owing to the high computational cost of diffusing an entire sequence at once.

Two primary approaches emerged to address the challenge of generating long sequences. TEDi [56] extends diffusion by incorporating a temporally varying noise level within the forward process while ignoring the reverse. Other methods [15, 31, 41, 46, 58] condition only the reverse process on previously estimated clean frames, ignoring the forward (Fig. 2 (b)). Although these approaches generate long sequences, their autoregressive nature com-

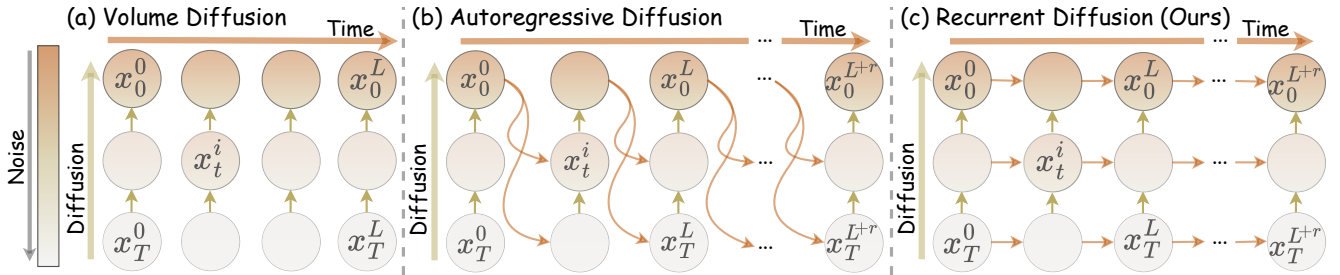


Figure 2. **Temporal diffusion models inference.** a) Volume diffusion treats the entire sequence as a monolithic input and diffuses it as a whole. b) Autoregressive diffusion conditions only the reverse process on previously estimated frames while ignoring the forward process. c) Recurrent diffusion leverages a recurrent formulation, explicitly conditions both forward and reverse processes on previous noisy frames.

plicates training and inference, as it necessitates fully denoising preceding frames to generate future frames.

To overcome these limitations, we propose *Recurrent Diffusion Model (RDM)*, a novel diffusion framework for generative temporal modelling. RDM leverages a recurrent formulation, analogous to Recurrent Neural Networks (RNNs) [23, 39] (Fig. 2 (c)). Within this recurrent formulation, both the forward (noise addition) and reverse (denoising) diffusion processes are explicitly conditioned on previous noisy frames. This design entangles denoising and future frame prediction tasks, removing restrictions on the generated sequences’ horizon. Note that removing recurrence turns RDM into a volume diffusion model. We will demonstrate that this “recurrence” improves results (Tab. 1) and significantly reduces computational complexity compared to baselines (Tab. 3).

Although this recurrent formulation offers compelling properties, a key challenge is preserving its probabilistic nature. This is because the recurrent transformation does not inherently guarantee valid probability distributions. Such deviations theoretically invalidate the diffusion model’s loss, thereby compromising training and leading to incorrect samples. To address this, we utilize normalizing flows [7, 37] to model temporal dependencies, thereby preserving the probability under recurrent transformations. In summary, our contributions are:

- A novel recurrent diffusion formulation that leverages Normalizing Flows to model spatiotemporal dependencies via noisy hidden states, establishing a non-Markovian framework for motion synthesis.
- A horizon-agnostic inference mechanism that decouples generation length from training constraints, enabling stable, open-ended sequence synthesis.
- An efficiency rollout strategy that reduces inference latency by skipping redundant diffusion steps, achieving significantly speedup over autoregressive baselines while maintaining motion fidelity.

These merits are demonstrated in text-to-motion generation tasks on the KIT-ML [35] and HumanML3D [12] datasets.

2. Related Work

2.1. Condition Motion Generation

Variational Auto-Encoders (VAEs) [25], have been widely used in human motion modelling. Notable works include Motion Transformation VAE (MT-VAE) [52], which decomposes motion into atomic units with an LSTM encoder-decoder, and Aliakbarian et al. [1], which integrates root variations with previous poses to reduce noise. Recently, MotionCLIP [44] introduces a transformer-based motion autoencoder, whereas AvatarCLIP [20] employs a volume rendering model for geometry and texture generation. TEMOS [34], similar to ACTOR [33], learns joint motion and text spaces with transformers. Lastly, Mo-Mask [14] models human motion as hierarchical tokens, with a Masked Transformer predicting base tokens from text and filling sequences during generation.

Despite their plausible results, VAE-based methods are often limited in their expressiveness due to inherent constraints imposed on the learned distributions.

In contrast to VAEs, Normalizing Flows (NFs) [37] train efficiently with exact maximum likelihood. Inspired by GLOW [24], MoGlow [17] proposes an autoregressive normalization network for motion sequences. However, while they offer decent results, normalizing flows are limited in their capacity to model complex distributions [26, 50].

Generative Adversarial Networks (GANs) [10] have been explored for motion generation. HP-GAN [2] uses a sequence-to-sequence model for probabilistic human motion prediction with a custom loss. Harvey et al. [16] address motion blurriness based on adversarial recurrent networks. Additionally, Wang et al. [49] decouples the generator into a smooth latent transition and a global skeleton decoder for individual latent frames. Although GANs do not impose explicit constraints on the target distribution, they are hard to train and often suffer from mode collapse [8, 27].

2.2. Diffusion Methods for Motion Generation

Inspired by non-equilibrium thermodynamics, Sohl-Dickstein et al. [42] propose a Markov chain that gradually

adds noise to data samples (*forward*) and learns to recover the noise with a neural network (*reverse*). After training, the reverse process resembles a generative model that generates samples from random noise. With the great success of diffusion models [18, 38], research began to shift to temporal data such as videos [4, 19], trajectory planning [3], and human motion [5, 54].

Volume diffusion. MotionDiffuse [54] is among the first to apply diffusion to text-to-motion generation using transformer generator networks on the SMPL pose space [29]. MLD [5] and MotionMamba [57] learn a latent space via a transformer VAE and apply diffusion within the latent space. MLD [5] used a transformer denoiser, whereas MotionMamba [57] proposes a state-space model (SSM) denoiser based on Mamba [6]. Using diffusion in the latent space enables them to train and sample orders of magnitude faster. However, this heavily depends on the quality of the latent space learned by the VAE, which requires careful tuning and regularization and can produce artefacts [21]. Recently, Light-T2M [53] exploits local and global sequence information and proposes an efficient Mamba denoiser architecture. They achieve SOTA performance while having only 10% of the size of MoMask [14].

Despite their success, these approaches generate a limited horizon, often short, temporal predictions [5, 54].

Autoregressive diffusion. TEDi [56] extends DDPM to the temporal dimension through temporally varying denoising. Therefore, during inference, TEDi gradually generates motion frames and feeds in newly noised frames. AMD [15] employs an autoregressive inverse process, which was an early effort to integrate temporal constraints into the diffusion process. DART [58] learns motion primitives in the latent space while UniPhys [51] encode variable motion frames into the latent space. Both use an autoregressive denoising process conditioned on previously estimated clean frames. Meng et al. [31] retain 3D features to ensure a uniform distribution before autoregressively denoising with a masked transformer. Meanwhile, CloSD [46] and A-MDM [41] implement an autoregressive denoising process conditioned on previously estimated frames in input pose space.

Autoregressive diffusion methods [15, 31, 41, 46, 58] condition the reverse denoising process on previously estimated clean frames, ignoring the forward process. While capable of generating long sequences, their autoregressive nature complicates training and inference, as they require fully denoising prior frames to produce future ones.

Inspired by recurrent networks [23, 39], we developed our *Recurrent Diffusion Model (RDM)* for temporal modelling, ensuring both forward and reverse processes follow temporal constraints by autoregressively adding and removing noise, departing from previous diffusion models [5, 15, 31, 41, 46, 54, 58]. Unlike Diffusion-Forcing [3],

the added noise is correlated, enabling the generation of sequences by sampling only the first segment. By leveraging normalizing flows [7, 24, 37] to model temporal transitions, our method captures more complex distributions than simple Gaussians, boosting capacity. RDM also skips diffusion steps during inference, reducing computational costs.

3. Background

3.1. Diffusion Models

Diffusion models [18, 42] add noise to data via a *forward process* and recover it through a *reverse process*, both following a Markov chain. Recently, diffusion has been used for text-to-motion generation [5, 54]. Given a pair $(x^{(j)}, u^{(j)})$, where $x^{(j)}$ is a sequence of poses and $u^{(j)}$ the description, each $x^{(j)}$ has F frames $(\theta^{i(j)})$ $i \in \{1, 2, \dots, F\}$, with $\theta^{i(j)} \in \mathbb{R}^D$ as the pose of the i -th frame. The reverse process $p_\theta(x_{t-1}|x_t)$ is modelled as a Gaussian transition learned with a neural network;

$$p_\theta(x_{0:T}) := p(x_T) \prod_{t=1}^T p_\theta(x_{t-1}|x_t)$$

$$p_\theta(x_{t-1}|x_t) := \mathcal{N}(x_{t-1}; \mu_\theta(x_t, t, \varphi(u^{(j)})), \Sigma_\theta(x_t, t, \varphi(u^{(j)}))) \quad (1)$$

Here, μ_θ and Σ_θ are parameterised by neural networks. φ is a pretrained neural network that extracts embeddings from the textual description $u^{(j)}$. The approximate posterior distribution $q(x_t|x_{t-1})$ of the diffusion model is called the *forward process* or *diffusion process*. It gradually adds Gaussian noise to the data according to a variance scheduler $\beta_1, \beta_2, \dots, \beta_T$, which can be learned [42] or fixed; (We removed the superscript j for clarity):

$$q(x_{1:T}|x_0) = \prod_{t=1}^T q(x_t|x_{t-1}) \quad (2)$$

$$q(x_t|x_{t-1}) := \mathcal{N}(x_t; \sqrt{1 - \beta_t}x_{t-1}, \beta_t \mathbf{I})$$

Training is performed by optimizing the Kullback-Leibler (KL) divergence between the forward and reverse processes. As suggested by Ho et al. [18] choosing a specific parametrization of $\mu_\theta(x_t, t, \varphi(u^{(j)}))$, yield the loss:

$$\mathcal{L}_\theta = \mathbb{E}_q \left[w(t) \|x - f_\theta(x_t, t, \varphi(u^{(j)}))\|^2 \right] \quad (3)$$

Here, $f_\theta(x_t, t, \varphi(u^{(j)}))$ is a learnable neural network, and the weight $w(t)$ can be freely specified. Efficient training can be achieved using Monte Carlo integration to approximate the expectation. We uniformly sample the time step t and minimize the loss using stochastic gradient descent.

3.2. Normalizing Flows

A normalizing flow [37] is a transformation $Y = f(X)$ that transforms one random variable X into another Y via suc-

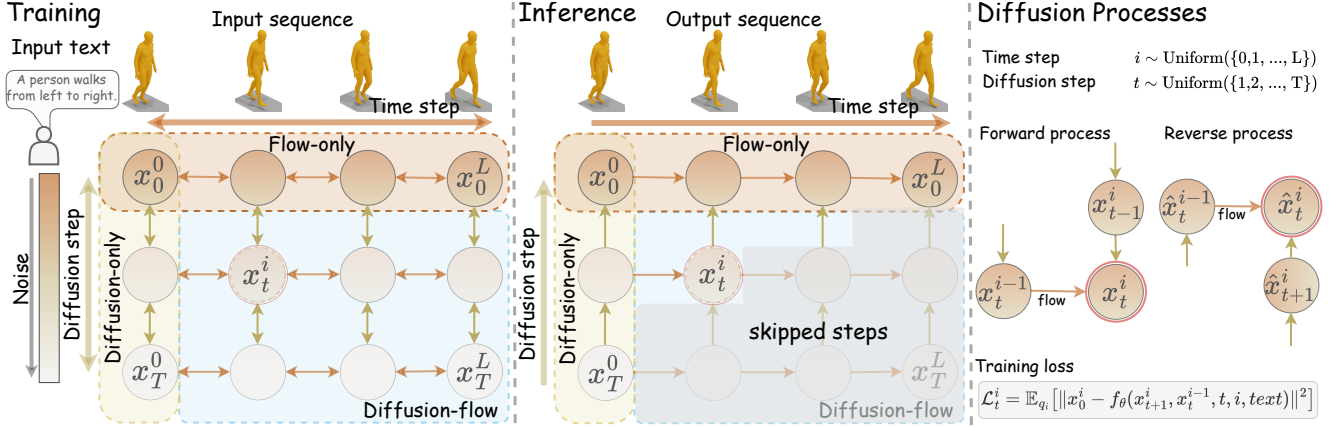


Figure 3. **Method overview:** Recurrent Diffusion Model (RDM) extends diffusion into the temporal dimension via a recurrent formulation, where each diffusion step is conditioned on the previous step within the same and previous segment. A key challenge is that recurrent transformations do not guarantee a valid training loss. RDM solves this by modelling transformations as invertible normalizing flows [7]. This creates a 2D grid with three regions: “Flow-only”, applied to clean segments, models temporal transitions with an invertible flow without diffusion; “Diffusion-only”, used exclusively for the initial segment (x_0^0), performs standard noising and denoising without flow interaction; and “Diffusion-flow”, applied to subsequent segments (x_t^i), recursively conditions on the previous diffused states x_{t-1}^i and x_t^{i-1} . During training, RDM uniformly samples a diffusion step t and a temporal step i and minimizes our simple loss (Eq. (13)). During inference, RDM skips diffusion steps, significantly reducing computational costs compared to baselines.

cessive volume-preserving, invertible and bijective transformations (Eq. (4)).

We use normalizing flows for modelling temporal human motion. Given a data point $x^{(j)}$ with F frames from a distribution $q(\mathcal{X})$, we split it into L segments $\{x^i\}_{i=0}^L$, each with equal length. Normalizing flow predicts the next segment distribution $x^{i+1} \sim P_{X^{i+1}}$ from the previous $x^i \sim P_{X^i}$. Applying the change of variable theorem, we obtain:

$$x^{i+1} = x_K = f_K \circ f_{K-1} \circ \dots \circ f_1(x^i) \quad (4)$$

$$P_{X^{i+1}}(x^{i+1}) = P_{X^{i+1}}(x^i) \prod_{k=1}^K \left| \det \left(\frac{\partial f_k(x_{k-1})}{\partial x_{k-1}} \right) \right|^{-1} \quad (5)$$

Samples from the transformed distribution $P_{X^{i+1}}$ are generated by sampling from the base distribution $x^i \sim P_{X^i}$, then applying the transformations in Eq. (4) to get x^{i+1} .

4. Recurrent Diffusion Model

We extend diffusion models [18, 42] into the temporal dimension by establishing a recurrent diffusion structure. Specifically, each diffusion step in both processes relies on the preceding diffusion step within the same temporal step and the corresponding diffusion step from the previous frames. This interconnectedness forms a 2D grid see Fig. 3.

However, a critical challenge arises: recurrent transformations do not inherently guarantee valid probability distributions. This theoretically invalidates the diffusion model’s loss as the KL divergence between the forward and reverse

processes becomes undefined. This renders the training loss (Eq. (3)) invalid and produces incorrect samples. To address this, we model temporal transitions with normalizing flows [7, 37], thereby preserving the probability.

In the subsequent sections, we detail the forward and reverse processes and how the training loss is obtained.

4.1. Forward Process

Given a sequence and text data sample pair $(x^{(j)}, u^{(j)})$, we begin by splitting each sequence into L segments, denoted as $\{x_0^i\}_{i=0}^L$, each of equal length.

For the initial segment, x_0^0 , RDM applies Gaussian noise in a manner consistent with prior diffusion models; this process is termed “diffusion-only”. In contrast, for all subsequent segments $\{x_t^i, i > 0\}$, our approach diverges from previous works [18, 42]. Here, RDM adds noise following the “diffusion-flow” as illustrated in Fig. 3. Within the “diffusion-flow” noise addition is conditioned on the previously diffused segment within the same temporal step (x_{t-1}^i) and the previous temporal step (x_t^{i-1}).

To obtain the noisy grid samples $\{x_t^i\}_{i=0}^L$ for $t = 1, \dots, T$, RDM first computes x_0^t within the “diffusion-only” then applies normalizing flow to the corresponding temporal step. Consistent with Jonathan et al. [18], the step size is controlled by the variance scheduler $\beta_t \in (0, 1)_{t=0}^T$ for $t = 0, \dots, T$. The approximate posterior is defined as:

$$q(x_{1:T}^i | x_0^i) = \prod_{i=1}^L \prod_{t=1}^T q(x_t^i | x_{t-1}^i, x_t^{i-1}) \quad (6)$$

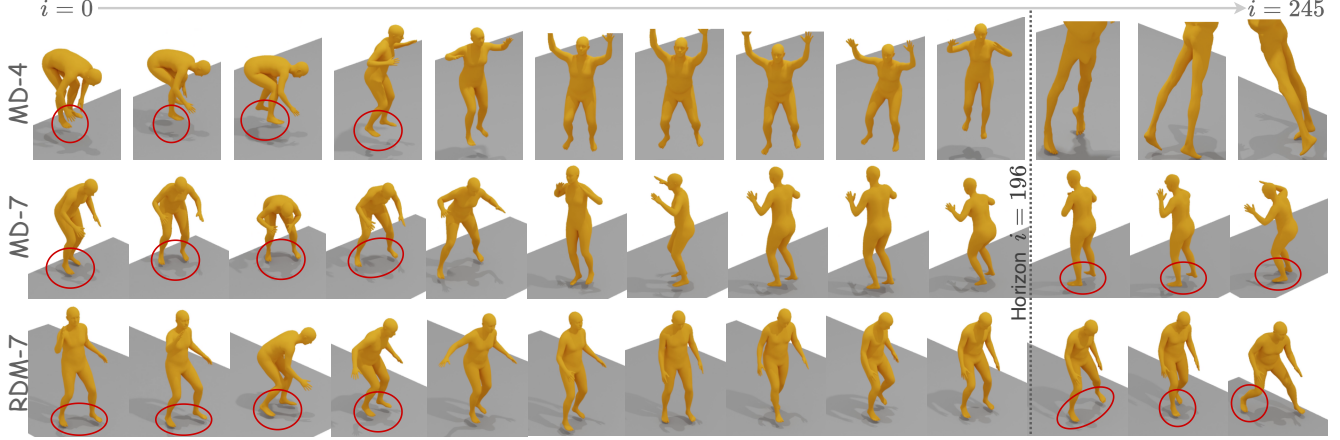


Figure 4. **Qualitative rollout results on the HumanML3D dataset [12].** To evaluate rollout performance, we used the prompt “A person is dribbling with a basketball”, generating motion up to 245 frames (right of the dashed line). Within the training horizon (left of the dashed line), all methods produce plausible motion, although MD-4 exhibits foot contact issues (red circles), unlike MD-7 and our RDM-7. Beyond the training horizon, MD-4 fails completely. Both MD-7 and RDM-7 generate sequences resembling the input; however, MD-7’s motion lacks coherence, while RDM-7 maintains greater coherence.

4.2. Reverse Process

The generative process follows the reverse of the 2D grid. While the “diffusion-only” reverse process uses the formulation from [18, 42], for “diffusion-flow” segments $\{x_{t-1}^i, i > 0\}$, leverages temporal relations. Specifically, the generative distribution depends on the previous diffusion step (x_t^i) and the previous temporal segment (x_{t-1}^{i-1}), as outlined by the following equations:

$$p_\theta(x_{1:T}^i | x_0^i, x_T^{i-1}) = \prod_{t=1}^T p_\theta(x_{t-1}^i | x_t^i, x_{t-1}^{i-1}) \quad (7)$$

$$p_\theta(x_{0:T}^L) = p(x_T^0) \prod_{i=1}^L \prod_{t=1}^T p_\theta(x_{t-1}^i | x_t^i, x_{t-1}^{i-1}) \quad (8)$$

In the “diffusion-only” segments, with a small β_t , the reverse distribution is Gaussian [9, 42], requiring only mean and variance estimation. Conversely, for “diffusion-flow”, the distribution $q(x_t^i | x_{t-1}^i, x_{t-1}^{i-1})$ is unknown because of the nonlinear flow transformations. Consequently, the reverse distribution $p_\theta(x_{t-1}^i | x_t^i, x_{t-1}^{i-1})$ is also unknown, which presents a challenge for sampling.

To sample from this intractable distribution, RDM exploits the invertibility of normalizing flows [37]. It inverts the step to “diffusion-only” where distributions are Gaussian, then samples and applies the forward flow to reach the target temporal step, as depicted next:

$$x_{t-1}^0 := \mathcal{N}(x_{t-1}^0, f_\phi^{(-i)}(\mu_\theta(x_t^i, x_{t-1}^{i-1}, t, i, \varphi(u^{(j)})), (1 - \bar{\alpha}_t)\mathbf{I})) \quad (9)$$

$$x_{t-1}^i = f_\phi^{(i)}(x_{t-1}^0) \quad (10)$$

where μ_θ is a learnable neural network (denoiser), both $(-i)$ and (i) indicate traversing the inverse and forward flow i times, respectively, f_ϕ represents the flow model parameterized by ϕ . φ is a pretrained CLIP model [36] that extracts embeddings from the textual description.

4.3. Normalizing Flow

We use a real-valued non-volume preserving (Real-NVP) [7] as a probabilistic transformation, as depicted in the following equation:

$$\begin{aligned} [\sigma_\phi, \mu_\phi] &= f_\phi(x_0^{i-1}, \varphi(u^{(j)})) \\ x_0^i &= x_0^{i-1} \odot \sigma_\phi(x_0^{i-1}, \varphi(u^{(j)})) + \mu_\phi(x_0^{i-1}, \varphi(u^{(j)})), \end{aligned} \quad (11)$$

where \odot is element-wise multiplication, and both σ_ϕ and μ_ϕ are deep feed-forward networks.

4.4. Training

During training, RDM maximizes the variational lower bound (VLB) of the log-likelihood of the 2D grid, which is simplified to (see Sec. 16 for full derivation):

$$\begin{aligned} \mathcal{L}_{VLB} &= \underbrace{D_{kl}(q(x_T^{0:L} | x_0^{0:L}) || p_\theta(x_T^{0:L}))}_{\mathcal{L}_T^{0:L}} \\ &+ \sum_{t=2}^T \underbrace{D_{kl}(q(x_{t-1}^{0:L} | x_t^{0:L}, x_0^{0:L}) || p_\theta(x_{t-1}^{0:L} | x_t^{0:L}))}_{\mathcal{L}_{t-1}^{0:L}} \\ &+ \mathbb{E}_q[\underbrace{-\log(p_\theta(x_0^{0:L} | x_1^{0:L}))}_{\mathcal{L}_0^{0:L}}] \end{aligned} \quad (12)$$

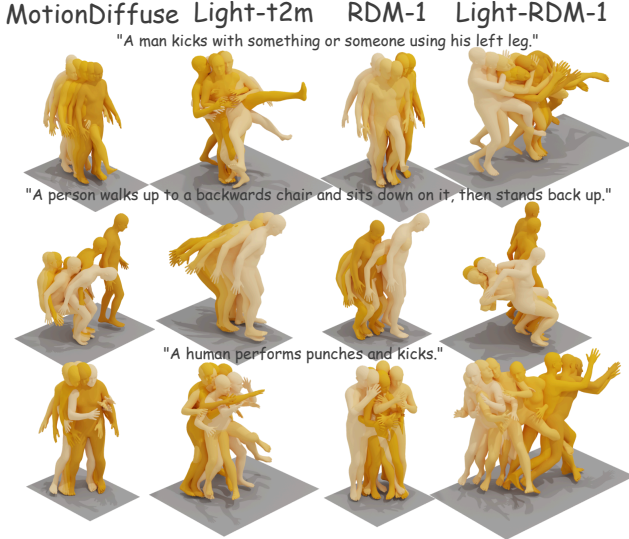


Figure 5. **Qualitative comparison of “volume” methods on HumanML3D [12].** Showing MotionDiffuse [54], SOTA Light-T2M [53], and our methods (Light/RDM-1) are comparable and aligned with prompts.

KL computation. The KL terms \mathcal{L}_{t-1}^0 within the “diffusion-only” segments are straightforward, following Gaussian distributions; RDM computes them in closed form, similar to Jonathan et al. [18]. In contrast, the intermediate KL terms $\mathcal{L}_{t-1}^{1:L}$ pose a significant challenge because they follow unknown distributions, which is a consequence of the nonlinear flow transformations.

Learning the posterior of unknown distributions often requires methods like Markov Chain Monte Carlo (MCMC) [32, 48], but with 1000 diffusion steps, these are infeasible due to slow convergence. This raises a crucial question: how can we efficiently learn the reverse process?

To train efficiently, RDM uses the invertibility of normalizing flows (Sec. 3.2) to derive a closed-form loss. It employs inverse flow to map predicted samples from frame i back to frame 0 (“diffusion-only”), where distributions are Gaussian, then computes KL in closed-form. The result is then transformed back to step i via the forward flow.

Consistent with Jonathan et al. [18], we learn only the mean of the distribution and fix the variance to $\sigma_t = \beta_t$. This approach yields a formula similar to that of [18], with additional weighting terms $|\det \frac{\partial f}{\partial x_0^i}|^{-1}$:

$$\mathcal{L}_{t-1}^i = \mathbb{E}_q \left[w(t) \left| \det \frac{\partial f_\phi}{\partial x_0^i} \right|^{-1} \|x_0^i - f_\theta(x_t^i, x_{t-1}^i, t, i)\|^2 \right] \quad (13)$$

Here, x_0^i is the clean segment at temporal step i and f_θ is a learnable neural network that predicts a clean segment; refer to Sec. 16 for a full derivation.

Training protocol. We learn both the flow and the de-

noiser jointly, using the expectation in Eq. (13), computed by means of Monte Carlo integration and uniformly sample random diffuse step t and temporal step i , then traversing the flow to reach the temporal location (see Fig. 3).

Sampling. Unlike previous methods [15, 31, 41, 46, 58], RDM does not require fully denoising previous segments to denoise the current one. Instead, using the flow, RDM skips diffusion steps by sampling in a staircase across the 2D grid (Fig. 3). Empirically, we found that starting the staircase at the denoising step equals the number of segments, balances computational complexity and sampling quality. (see Sec. 11 and 12 for details).

5. Experiments

The primary objective of our evaluation is to quantify the performance of the rollout diffusion framework. Unlike volume-diffusion methods, which model motion as a whole, the rollout problem is more complex as it accumulates error over time. We chose to perform denoising in pose space. This choice, informed by the architectures of MotionDiffuse (MD) [54] and Light-T2M [53], grants the flexibility required to ablate segment lengths and sequence counts.

Rollout diffusion baselines. Autoregressive diffusion models such as AMD [15], CLoS (DIP) [46], and A-MDM [41] can generate motion beyond the training horizon due to their recursive reverse process, making them rollout baselines. However, they only report results on HumanML3D [12]. Therefore, we trained a MotionDiffuse (MD) [54] based baselines for a fairer comparison. TEDi [56] and UniPhys [51] are trained on different datasets and were not compared.

The MD baseline predicts the next clean motion segments from corrupted inputs. We implement “MD-4” and “MD-7”, using 4 and 7 segments, respectively, as non-recurrent counterparts to our framework. These “MD- x ” variants essentially function as ablations of our model, where the recurrent connections are removed, and diffusion is applied independently to each segment.

Volume diffusion baselines. We compare our volume diffusion approach with SOTA volume methods, including MDM [45], MotionDiffuse [54], MLD [5], MotionMamba [57], ReMoDiffuse [55], and Light-T2M [53]. We also report results of non-diffusion methods TEMOS [34], T2M [13] and MoMask [14].

Qualitative evaluation. Fig. 5 and 4 show our methods produce plausible motions from input captions. To evaluate rollout, we use open-ended descriptions, prompting the model to create continuous, meaningful motion beyond horizon. These motions are visually inspected for failures.

In Fig. 4, with the prompt “A person is dribbling with a basketball”, we extend motion beyond the training horizon to compare MD-4, MD-7, and RDM-7. Within the training horizon (left of the dashed line), all produce plausible

Framework	Method	R-Precision (\uparrow)			FID (\downarrow)	MultiModal Dist (\downarrow)	MultiModality (\uparrow)
		Top 1	Top 2	Top 3			
	Real motion	0.511 \pm .003	0.703 \pm .002	0.797 \pm .003	0.002 \pm .000	2.974 \pm .008	-
VAE	TEMOS [34]	0.424 \pm .002	0.612 \pm .002	0.722 \pm .002	3.734 \pm .028	3.703 \pm .008	0.368 \pm .018
	T2M [13]	0.457 \pm .002	0.639 \pm .003	0.740 \pm .003	1.067 \pm .002	3.340 \pm .008	2.090 \pm .083
	MoMask [14]	0.521 \pm .002	0.713 \pm .002	0.807 \pm .002	0.045 \pm .002	2.958 \pm .008	1.241 \pm .040
	MDM [45]	0.320 \pm .005	0.498 \pm .004	0.611 \pm .007	0.544 \pm .044	5.566 \pm .027	2.799 \pm .072
Volume Diffusion	MotionDiffuse [54]	0.491 \pm .001	0.681 \pm .001	0.782 \pm .001	0.630 \pm .001	3.113 \pm .001	1.553 \pm .042
	MLD [5]	0.481 \pm .003	0.673 \pm .003	0.772 \pm .002	0.473 \pm .013	3.196 \pm .010	2.413 \pm .079
	MotionMamba [57]	0.502 \pm .003	0.693 \pm .002	0.792 \pm .002	0.281 \pm .009	3.060 \pm .058	2.294 \pm .058
	ReMoDiffuse [55]	0.510 \pm .005	0.698 \pm .006	0.795 \pm .004	0.103 \pm .004	2.974 \pm .016	1.795 \pm .043
	Light-T2M [53]	0.511 \pm .003	0.699 \pm .002	0.795 \pm .002	0.040 \pm .002	3.002 \pm .008	1.670 \pm .061
	RDM-1 (ours)	0.449 \pm .001	0.661 \pm .001	0.777 \pm .001	0.585 \pm .001	3.113 \pm .001	1.538 \pm .042
	Light-RDM-1 (ours)	0.510 \pm .006	0.699 \pm .003	0.794 \pm .002	0.07 \pm .003	3.005 \pm .008	1.713 \pm .074
	AMD [15]	-	-	0.617 \pm .014	0.586 \pm .107	5.469 \pm .063	2.512 \pm .232
Rollout Diffusion	CLoSD (DiP) [46]	0.463 \pm .006	0.668 \pm .006	0.773 \pm .008	0.247 \pm .034	3.178 \pm .025	-
	A-MDM [41]	-	-	-	1.7435 \pm .0813	-	-
	MD-4	0.339 \pm .005	0.499 \pm .006	0.605 \pm .007	4.414 \pm .116	4.338 \pm .031	2.262 \pm .155
	MD-7	0.368 \pm .002	0.546 \pm .007	0.658 \pm .007	3.377 \pm .0	4.019 \pm .03	1.771 \pm .145
	RDM-4 (ours)	0.442 \pm .006	0.664 \pm .004	0.762 \pm .004	0.312 \pm .016	3.604 \pm .006	1.544 \pm .046
	RDM-7 (ours)	0.455 \pm .002	0.653 \pm .003	0.772 \pm .002	0.272 \pm .018	3.651 \pm .008	1.199 \pm .04

Table 1. **Quantitative results on the HumanML3D [12] test set.** All methods use ground truth motion length. Evaluations were run 20 times with 95% CI. Rows are colour-coded as **best**, **second best**, and **third best**. Our recurrent methods (RDM-4/7) outperform rollout baselines significantly and are comparable to CLoSD (DiP) [46]. Our volume methods (Light-RDM-1) achieves on par results with MotionDiffuse [54] and SOTA Light-T2M [53].

Framework	Method	R-Precision (\uparrow)			FID (\downarrow)	MultiModal Dist (\downarrow)	MultiModality (\uparrow)
		Top 1	Top 2	Top 3			
	Real motion	0.5138	0.6957	0.7937	0.002 \pm .000	2.974 \pm .008	-
VAE	TEMOS [34]	0.353 \pm .006	0.561 \pm .007	0.687 \pm .005	3.717 \pm .051	3.417 \pm .019	0.532 \pm .034
	T2M [13]	0.370 \pm .005	0.569 \pm .007	0.693 \pm .007	2.770 \pm .109	3.401 \pm .008	1.482 \pm .065
	MoMask [14]	0.433 \pm .007	0.656 \pm .005	0.781 \pm .005	0.204 \pm .011	2.779 \pm .022	1.131 \pm .043
	MDM [45]	0.164 \pm .004	0.291 \pm .004	0.396 \pm .004	0.497 \pm .021	9.191 \pm .022	1.907 \pm .214
Volume Diffusion	MotionDiffuse [54]	0.417 \pm .004	0.621 \pm .004	0.739 \pm .004	1.954 \pm .062	2.958 \pm .005	0.730 \pm .013
	MLD [5]	0.390 \pm .008	0.609 \pm .008	0.734 \pm .007	0.404 \pm .027	3.204 \pm .027	2.192 \pm .071
	MotionMamba [57]	0.419 \pm .006	0.645 \pm .005	0.765 \pm .006	0.307 \pm .041	3.021 \pm .025	1.678 \pm .064
	ReMoDiffuse [55]	0.427 \pm .014	0.641 \pm .004	0.765 \pm .055	0.155 \pm .006	2.814 \pm .012	1.239 \pm .028
	Light-T2M [53]	0.444 \pm .006	0.670 \pm .007	0.794 \pm .005	0.161 \pm .009	2.746 \pm .016	1.005 \pm .036
	RDM-1 (ours)	0.381 \pm .004	0.603 \pm .004	0.734 \pm .004	1.8151 \pm .062	2.958 \pm .005	0.693 \pm .013
	Light-RDM-1 (ours)	0.443 \pm .005	0.665 \pm .007	0.791 \pm .005	0.299 \pm .02	2.772 \pm .013	1.05 \pm .050
	MD-4	0.3067 \pm .007	0.4816 \pm .007	0.6085 \pm .007	2.8553 \pm .073	4.1278 \pm .026	2.9595 \pm .086
Rollout Diffusion	MD-7	0.2728 \pm .004	0.4528 \pm .0059	0.5794 \pm .005	5.5562 \pm .085	4.5790 \pm .03	2.4437 \pm .1054
	RDM-4 (ours)	0.364 \pm .008	0.576 \pm .008	0.712 \pm .006	1.95 \pm .051	3.541 \pm .02	1.068 \pm .045
	RDM-7 (ours)	0.377 \pm .005	0.5913 \pm .003	0.715 \pm .005	1.819 \pm .05	3.412 \pm .016	0.59 \pm .038

Table 2. **Quantitative results on the KIT-ML [35] test set.** All methods use ground truth motion length. Evaluations were run 20 times with 95% CI. Rows are colour-coded as **best**, **second best**, and **third best**. Our recurrent methods (RDM-4/7) significantly outperform rollout baselines. MD-x baselines degrade with more segments, because the dataset features shorter sequences (max 196 frames), which harms future segment prediction. Volume diffusion models generally outperform rollout methods. Our volume methods (RDM-1/Light-RDM-1) achieves comparable results with MotionDiffuse [54] and SOTA Light-T2M [53].

motion, but MD-4 exhibits foot contact issues (red circles), a problem not observed in MD-7 or RDM-7. Beyond the training horizon (right of the dashed line), MD-4 fails to produce plausible motion, while MD-7 and RDM-7 generate sequences that reasonably match the input prompt. Nevertheless, we observe that RDM-7’s motions are more coherent than MD-7, and significantly faster (see Tab. 3). Static images do not accurately convey motion quality; we

recommend that the reader view our supplementary video.

Quantitative evaluation. Analyzing rollout methods in Tab. 1 and 2 shows MD-4/7 are strong baselines with 0.658 R-Top3, comparable to AMD [15]. Our RDM-4/7 outperform MD-x and other baselines except CLoSD (DiP) [46] on HumnaML3D [12] and KIT-ML [35], highlighting the importance of a recurrent connection. We further observe that the performance of MD-x baselines de-

Framework	Method	Total Inference Time (s) ↓					FLOPs (T) ↓					Parameters
		DDIM				DDPM	DDIM				DDPM	
		10	50	100	200	1000	10	50	100	200	1000	
Volume Diffusion	MotionDiffuse [54]	—	2.71±0.23	4.92±.04	9.79±.08	52.07±2.06	—	64.64	128.44	256.02	1276.71	$x \in \mathbb{R}^{196 \times 251}$
	CLoSD (DiP) [46]	1.77±.037	8.73±.03	17.5±.09	34.87±.04	(93.18±.16)	45.89	229.44	458.88	917.76	(2617.93)	$x \in \mathbb{R}^{40 \times 251}$
Rollout Diffusion	MD-7	—	5.40±.08	11.39±.80	21.34±.09	113.20±4.63	—	83.41	165.97	331.08	1652.01	$x \in \mathbb{R}^{28 \times 251}$
	RDM-4 (ours)	0.21±.007	1.95±1.71	2±1.19	3.26±1.51	10.89±2.11	0.275	0.282	0.458	0.809	3.62	$x \in \mathbb{R}^{49 \times 251}$
	RDM-7 (ours)	0.59±.005	2.61±1.75	2.48±1.19	3.86±1.49	11.7±2.02	0.66	0.533	0.644	0.866	2.32	$x \in \mathbb{R}^{28 \times 251}$
	RDM-14 (ours)	0.20±.005	4.26±0.80	3.66±.06	5.2±.79	13.17±1.4	0.162	3	3.07	3.21	1.48	$x \in \mathbb{R}^{14 \times 251}$

Table 3. **Inference time comparison.** Rows are colour-coded as **best**, **second best**, and **third best**. Our method skips diffusion steps via “staircase sampling”, reducing inference time and FLOPs compared to volume methods that process the entire sequence. RDM is more efficient than rollout baselines (MD-x/CLoSD [46]) because it does not fully denoise previous frames to generate new ones.

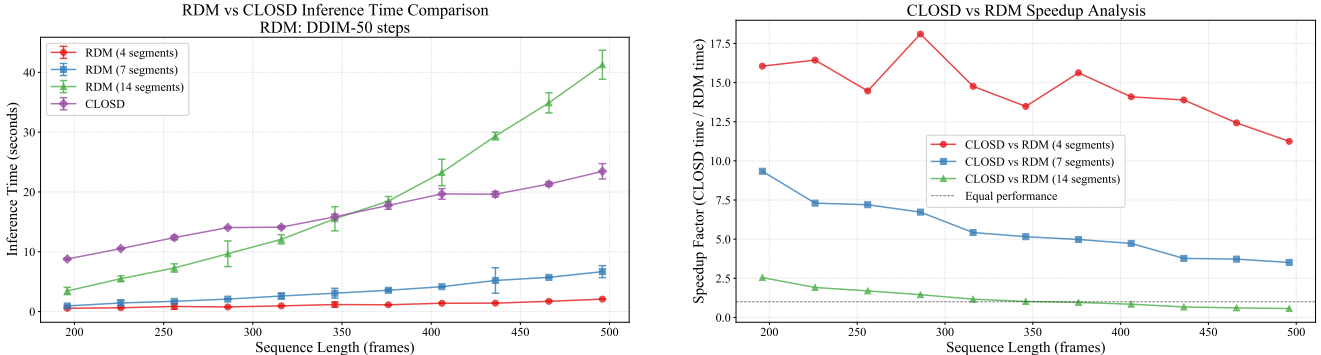


Figure 6. **Comparison of computational efficiency between RDM and CLoSD (DiP) [46].** (left) Inference time vs. sequence length for RDM with 4, 7, 14 segments (DDIM-50 steps) and CLoSD. Error bars show ± 3 standard deviations. (right) Speedup analysis dividing CLoSD inference time by RDM’s. RDM-4/7 outperforms CLoSD by $(3.51 \text{ to } 18.11) \times$ across sequence lengths, with higher speedups for shorter sequences. Speedup varies with segment configuration: RDM-4 is faster than RDM-7, RDM-14 is slowest.

clines with more segments, especially on KIT-ML, because they feature shorter sequences than the 196-frame maximum training length, making future prediction harder. In line with this, HumanML3D predominantly contains longer sequences, as shown in Tab. 1, we do not observe a performance decline with larger segment baselines. Our RDM-4/7 achieves a comparable Top-3 precision to CLoSD (DiP), which achieves slightly better FID score on HumnaML3D.

As evident in Tab. 1 and 2, volume methods outperform rollouts, with RDM-1 and Light-RDM-1 achieving results comparable to MotionDiffuse [54] and SOTA Light-T2M [53] on KIT-ML and HumanML3D. Their generation is limited to training horizon.

Inference time. RDM accelerates inference by skipping diffusion steps, maintaining compatibility with DDIM sampling [43]. As shown in Tab. 3, RDM variants achieve lower FLOPs and significantly reduced wall-clock times compared to MotionDiffuse [54] and CLoSD[46]. Using DDIM-50 to balance fidelity and speed, we evaluate scaling properties in Fig. 6. RDM-4 is the most efficient configuration, delivering a $11.25 \times$ to $18.11 \times$ speedup over CLoSD, followed by RDM-7 at $3.51 \times$ to $9.34 \times$. In contrast, RDM-14 provides a modest $0.57 \times$ to $2.55 \times$ improvement.

Efficiency is inherently tied to segment configuration and

sequence length; while most variants scale favorably, RDM-14’s overhead leads to diminished returns beyond the 350-frame threshold (see Sec. 11 and 12). These benchmarks were conducted on an NVIDIA H100 GPU using KIT-ML data, with results averaged over 20 trials. Detailed comparative analyses are available in Appendix 12. **Limitations.** Although RDM can generate sequences beyond the training horizon, its numerical stability depends on the flow, which is challenging with many segments. Additionally, generated frames become noisier over time, especially with a few recurrence steps. (See Sec. 10.1)

6. Conclusion

We introduce Recurrent Diffusion Model (RDM), a framework extending diffusion into the temporal domain with a recurrent formulation. It enforces temporal constraints by recurrently adding and removing noise. RDM’s volume method matches SOTA volume results. While the recurrent version is on par with autoregressive diffusion, it generates sequences beyond the training horizon with significantly lower inference complexity. We believe RDM advances temporal diffusion models and naturally extends into the latent space, though these avenues remain for future research.

Acknowledgements

The research presented here has been supported by the UCL Centre for Doctoral Training in Foundational AI under UKRI grant number EP/S021566/1. The authors are grateful to the Baskerville Tier 2 HPC service (<https://www.baskerville.ac.uk/>). Funded by the EP-SRC and UKRI through the World Class Labs scheme (EP/T022221/1) and the Digital Research Infrastructure programme (EP/W032244/1), it is operated by Advanced Research Computing at the University of Birmingham. We thank Shalini Maiti, Abdallah Basheir, Wonbong Jang, Oscar Key, and Waleed Dawood for their fruitful discussions and valuable feedback.

References

- [1] Sadeh Aliakbarian, Fatemeh Sadat Saleh, Mathieu Salzmann, Lars Petersson, and Stephen Gould. A stochastic conditioning scheme for diverse human motion prediction. In *Proceedings of the IEEE/CVF Conference on Computer Vision and Pattern Recognition (CVPR)*, 2020. 2
- [2] Emad Barsoum, John Kender, and Zicheng Liu. HP-GAN: probabilistic 3d human motion prediction via GAN. *CoRR*, 2017. 2
- [3] Boyuan Chen, Diego Martí Monsó, Yilun Du, Max Simchowitz, Russ Tedrake, and Vincent Sitzmann. Diffusion forcing: Next-token prediction meets full-sequence diffusion. In *Advances in Neural Information Processing Systems*, 2024. 3
- [4] Weifeng Chen, Jie Wu, Pan Xie, Hefeng Wu, Jiashi Li, Xin Xia, Xuefeng Xiao, and Liang Lin. Control-a-video: Controllable text-to-video generation with diffusion models, 2023. 3
- [5] Xin Chen, Biao Jiang, Wen Liu, Zilong Huang, Bin Fu, Tao Chen, and Gang Yu. Executing your commands via motion diffusion in latent space. In *Proceedings of the IEEE/CVF Conference on Computer Vision and Pattern Recognition*, 2023. 1, 3, 6, 7, 2
- [6] Tri Dao and Albert Gu. Transformers are SSMS: Generalized models and efficient algorithms through structured state space duality. In *International Conference on Machine Learning (ICML)*, 2024. 3
- [7] Laurent Dinh, Jascha Sohl-Dickstein, and Samy Bengio. Density estimation using real NVP. In *International Conference on Learning Representations*, 2017. 2, 3, 4, 5, 1
- [8] Ricard Durall, Avraam Chatzimichailidis, Peter Labus, and Janis Keuper. Combating mode collapse in gan training: An empirical analysis using hessian eigenvalues. *ArXiv*, 2020. 2
- [9] William Feller. On the theory of stochastic processes, with particular reference to applications. 1949. 5
- [10] Ian Goodfellow, Jean Pouget-Abadie, Mehdi Mirza, Bing Xu, David Warde-Farley, Sherjil Ozair, Aaron Courville, and Yoshua Bengio. Generative adversarial nets. In *Advances in Neural Information Processing Systems*, 2014. 2
- [11] Chuan Guo, Xinxin Zuo, Sen Wang, Shihao Zou, Qingyao Sun, Annan Deng, Minglun Gong, and Li Cheng. Action2motion: Conditioned generation of 3d human motions. In *Proceedings of the 28th ACM International Conference on Multimedia*, pages 2021–2029, 2020. 1
- [12] Chuan Guo, Shihao Zou, Xinxin Zuo, Sen Wang, Wei Ji, Xingyu Li, and Li Cheng. Generating diverse and natural 3d human motions from text. In *Proceedings of the IEEE/CVF Conference on Computer Vision and Pattern Recognition (CVPR)*, pages 5152–5161, 2022. 2, 5, 6, 7, 1, 3
- [13] Chuan Guo, Shihao Zou, Xinxin Zuo, Sen Wang, Wei Ji, Xingyu Li, and Li Cheng. Generating diverse and natural 3d human motions from text. In *2022 IEEE/CVF Conference on Computer Vision and Pattern Recognition (CVPR)*, 2022. 6, 7
- [14] Chuan Guo, Yuxuan Mu, Muhammad Gohar Javed, Sen Wang, and Li Cheng. Momask: Generative masked modeling of 3d human motions. In *Proceedings of the IEEE/CVF Conference on Computer Vision and Pattern Recognition*, 2024. 2, 3, 6, 7
- [15] Bo Han, Hao Peng, Minjing Dong, Chang Xu, Yi Ren, Yixuan Shen, and Yuheng Li. Amd autoregressive motion diffusion. *arXiv preprint arXiv:2305.09381*, 2023. 1, 3, 6, 7, 2
- [16] Félix G. Harvey, Mike Yurick, Derek Nowrouzezahrai, and Christopher Pal. Robust motion in-betweening. *ACM Trans. Graph.*, 2020. 2
- [17] Gustav Eje Henter, Simon Alexanderson, and Jonas Beskow. MoGlow: Probabilistic and controllable motion synthesis using normalising flows. *ACM Transactions on Graphics*, 2020. 2
- [18] Jonathan Ho, Ajay Jain, and Pieter Abbeel. Denoising diffusion probabilistic models. In *Advances in Neural Information Processing Systems*, pages 6840–6851. Curran Associates, Inc., 2020. 1, 3, 4, 5, 6, 8, 9
- [19] Jonathan Ho, Tim Salimans, Alexey Gritsenko, William Chan, Mohammad Norouzi, and David J Fleet. Video diffusion models. *arXiv:2204.03458*, 2022. 3
- [20] Fangzhou Hong, Mingyuan Zhang, Liang Pan, Zhongang Cai, Lei Yang, and Ziwei Liu. Avatarclip: Zero-shot text-driven generation and animation of 3d avatars. *ACM Trans. Graph.*, 2022. 2
- [21] Emiel Hoogeboom, Thomas Mensink, Jonathan Heek, Kay Lamerigts, Ruiqi Gao, and Tim Salimans. Simpler diffusion (sid2): 1.5 fid on imagenet512 with pixel-space diffusion. *arXiv preprint*, 2024. 3
- [22] Christian Horvat and Jean-Pascal Pfister. Denoising normalizing flow. In *Advances in Neural Information Processing Systems*, pages 9099–9111. Curran Associates, Inc., 2021. 1
- [23] M I Jordan. Serial order: a parallel distributed processing approach. technical report, june 1985-march 1986. 1986. 2, 3
- [24] Durk P Kingma and Prafulla Dhariwal. Glow: Generative flow with invertible 1x1 convolutions. In *Advances in Neural Information Processing Systems*. Curran Associates, Inc., 2018. 2, 3
- [25] Diederik P Kingma and Max Welling. Auto-encoding variational bayes. *arXiv preprint arXiv:1312.6114*, 2013. 1, 2
- [26] Polina Kirichenko, Pavel Izmailov, and Andrew G Wilson. Why normalizing flows fail to detect out-of-distribution

- data. In *Advances in Neural Information Processing Systems*, 2020. 2
- [27] Youssef Kossale, Mohammed Airaj, and Aziz Darouichi. Mode collapse in generative adversarial networks: An overview. In *2022 8th International Conference on Optimization and Applications (ICOA)*, 2022. 2
- [28] Ruilong Li, Shan Yang, David A. Ross, and Angjoo Kanazawa. Ai choreographer: Music conditioned 3d dance generation with aist++, 2021. 1
- [29] Matthew Loper, Naureen Mahmood, Javier Romero, Gerard Pons-Moll, and Michael J. Black. SMPL: A skinned multi-person linear model. *ACM Trans. Graphics (Proc. SIGGRAPH Asia)*, 34(6):248:1–248:16, 2015. 3
- [30] Naureen Mahmood, Nima Ghorbani, Nikolaus F. Troje, Gerard Pons-Moll, and Michael J. Black. AMASS: Archive of motion capture as surface shapes. In *International Conference on Computer Vision*, pages 5442–5451, 2019. 1
- [31] Zichong Meng, Yiming Xie, Xiaogang Peng, Zeyu Han, and Huaizu Jiang. Rethinking diffusion for text-driven human motion generation. *arXiv*, 2024. 1, 3, 6
- [32] N. Metropolis, A. W. Rosenbluth, M. N. Rosenbluth, A. H. Teller, and E. Teller. Equation of state calculations by fast computing machines. *Journal of Chemical Physics*, 1953. 6, 9
- [33] Mathis Petrovich, Michael J. Black, and Gül Varol. Action-conditioned 3D human motion synthesis with transformer VAE. In *International Conference on Computer Vision (ICCV)*, 2021. 2
- [34] Mathis Petrovich, Michael J. Black, and Gül Varol. Temos: Generating diverse human motions from textual descriptions. In *Computer Vision – ECCV 2022: 17th European Conference, Tel Aviv, Israel, October 23–27, 2022, Proceedings, Part XXII*, 2022. 1, 2, 6, 7
- [35] Matthias Plappert, Christian Mandery, and Tamim Asfour. The KIT motion-language dataset. *Big Data*, 4(4):236–252, 2016. 2, 7, 1, 3, 4
- [36] Alec Radford, Jong Wook Kim, Chris Hallacy, Aditya Ramesh, Gabriel Goh, Sandhini Agarwal, Girish Sastry, Amanda Askell, Pamela Mishkin, Jack Clark, Gretchen Krueger, and Ilya Sutskever. Learning transferable visual models from natural language supervision. In *Proceedings of the 38th International Conference on Machine Learning*, pages 8748–8763. PMLR, 2021. 5, 3
- [37] Danilo Rezende and Shakir Mohamed. Variational inference with normalizing flows. In *Proceedings of the 32nd International Conference on Machine Learning*, pages 1530–1538, Lille, France, 2015. PMLR. 2, 3, 4, 5
- [38] Robin Rombach, Andreas Blattmann, Dominik Lorenz, Patrick Esser, and Björn Ommer. High-resolution image synthesis with latent diffusion models. In *Proceedings of the IEEE/CVF Conference on Computer Vision and Pattern Recognition*, pages 10684–10695, 2022. 3
- [39] D. E. Rumelhart, G. E. Hinton, and R. J. Williams. *Learning Internal Representations by Error Propagation*, page 318–362. MIT Press, Cambridge, MA, USA, 1986. 2, 3
- [40] Fabian Schaipp, Ruben Ohana, Michael Eickenberg, Aaron Defazio, and Robert M. Gower. MoMo: Momentum models for adaptive learning rates. 2023. 3
- [41] Yi Shi, Jingbo Wang, Xuekun Jiang, Bingkun Lin, Bo Dai, and Xue Bin Peng. Interactive character control with autoregressive motion diffusion models. *ACM Trans. Graph.*, 2024. 1, 3, 6, 7
- [42] Jascha Sohl-Dickstein, Eric Weiss, Niru Maheswaranathan, and Surya Ganguli. Deep unsupervised learning using nonequilibrium thermodynamics. In *Proceedings of the 32nd International Conference on Machine Learning*, pages 2256–2265. PMLR, 2015. 1, 2, 3, 4, 5
- [43] Jiaming Song, Chenlin Meng, and Stefano Ermon. Denoising diffusion implicit models. In *International Conference on Learning Representations*, 2021. 8
- [44] Guy Tevet, Brian Gordon, Amir Hertz, Amit H Bermano, and Daniel Cohen-Or. Motionclip: Exposing human motion generation to clip space. In *Computer Vision–ECCV 2022: 17th European Conference, Tel Aviv, Israel, October 23–27, 2022, Proceedings, Part XXII*, pages 358–374. Springer, 2022. 1, 2
- [45] Guy Tevet, Sigal Raab, Brian Gordon, Yoni Shafir, Daniel Cohen-or, and Amit Haim Bermano. Human motion diffusion model. In *The Eleventh International Conference on Learning Representations*, 2023. 1, 6, 7
- [46] Guy Tevet, Sigal Raab, Setareh Cohan, Daniele Reda, Zhengyi Luo, Xue Bin Peng, Amit Haim Bermano, and Michiel van de Panne. CLoSD: Closing the loop between simulation and diffusion for multi-task character control. In *The Thirteenth International Conference on Learning Representations (ICLR)*, 2025. 1, 3, 6, 7, 8, 2, 5
- [47] Jonathan Tseng, Rodrigo Castellon, and C Karen Liu. Edge: Editable dance generation from music. *arXiv preprint arXiv:2211.10658*, 2022. 1
- [48] Maxime Vono, Daniel Paulin, and Arnaud Doucet. Efficient mcmc sampling with dimension-free convergence rate using admn-type splitting. *Journal of Machine Learning Research*, 2022. 6, 9
- [49] Zhenyi Wang, Ping Yu, Yang Zhao, Ruiyi Zhang, Yufan Zhou, Junsong Yuan, and Changyou Chen. Learning diverse stochastic human-action generators by learning smooth latent transitions. In *The Thirty-Fourth AAAI Conference on Artificial Intelligence AAAI*. AAAI Press, 2020. 2
- [50] Hao Wu, Jonas Köhler, and Frank Noe. Stochastic normalizing flows. In *Advances in Neural Information Processing Systems*, 2020. 2
- [51] Yan Wu, Korrawe Karunratanakul, Zhengyi Luo, and Siyu Tang. Uniphys: Unified planner and controller with diffusion for flexible physics-based character control. In *Proceedings of the IEEE/CVF International Conference on Computer Vision (ICCV)*, 2025. 3, 6
- [52] Xinchun Yan, Akash Rastogi, Ruben Villegas, Kalyan Sunkavalli, Eli Shechtman, Sunil Hadap, Ersin Yumer, and Honglak Lee. Mt-vae: Learning motion transformations to generate multimodal human dynamics. In *Computer Vision – ECCV 2018: 15th European Conference, Munich, Germany, September 8–14, 2018, Proceedings, Part V*, 2018. 2
- [53] Ling-An Zeng, Guohong Huang, Gaojie Wu, and Wei-Shi Zheng. Light-t2m: A lightweight and fast model for text-to-motion generation. *Proceedings of the AAAI Conference on Artificial Intelligence*, 2025. 3, 6, 7, 8, 1, 2

- [54] Mingyuan Zhang, Zhongang Cai, Liang Pan, Fangzhou Hong, Xinying Guo, Lei Yang, and Ziwei Liu. Motiondiffuse: Text-driven human motion generation with diffusion model. *IEEE Transactions on Pattern Analysis and Machine Intelligence*, 46:4115–4128, 2022. [1](#), [3](#), [6](#), [7](#), [8](#), [2](#), [4](#)
- [55] Mingyuan Zhang, Xinying Guo, Liang Pan, Zhongang Cai, Fangzhou Hong, Huirong Li, Lei Yang, and Ziwei Liu. Remodiffuse: Retrieval-augmented motion diffusion model. In *Proceedings of the IEEE/CVF International Conference on Computer Vision (ICCV)*, 2023. [6](#), [7](#), [3](#)
- [56] Zihan Zhang, Richard Liu, Kfir Aberman, and Rana Hanocka. Tedi: Temporally-entangled diffusion for long-term motion synthesis. In *SIGGRAPH, Technical Papers*, 2024. [1](#), [3](#), [6](#)
- [57] Zeyu Zhang, Akide Liu, Ian Reid, Richard Hartley, Bohan Zhuang, and Hao Tang. Motion mamba: Efficient and long sequence motion generation. In *European Conference on Computer Vision*, pages 265–282. Springer, 2025. [3](#), [6](#), [7](#), [1](#)
- [58] Kaifeng Zhao, Gen Li, and Siyu Tang. DartControl: A diffusion-based autoregressive motion model for real-time text-driven motion control. In *The Thirteenth International Conference on Learning Representations (ICLR)*, 2025. [1](#), [3](#), [6](#)

RDM: Recurrent Diffusion Model for Human Motion Generation

Supplementary Material

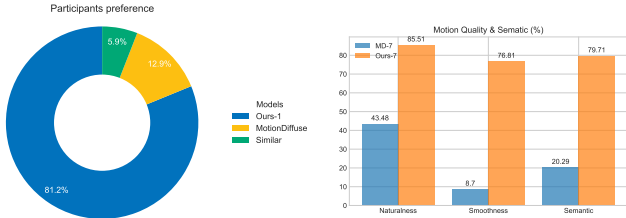


Figure 7. **User study analysis result.** Semantic in percentage denotes how well the motion visually corresponds to the input sentences. Motion quality in percentage shows the overall quality of motion in terms of naturalness. Smoothness in percentage, showing how good the overall motion smoothness and coherence. (A higher value is better.) Our method’s score, denoted in *Ours-7* (RDM-7), has the highest percentage compared to the baseline.

7. User study.

To further evaluate the quality of the generated motion, we conducted a user study to observe the subjective quality of the generated motion using our method and baselines. We asked 85 participants to rank 11 motion sequences from our method and baselines, based on quality of motion, alignment to the input sentence, naturalness, and smoothness. The four methods of rollout and volume diffusion are *ours-7*, *MD-7*, *ours-1*, and motion diffusion.

We quantified the user study with two preference scores; the first to evaluate the rollout (*ours-7* and *MD-7*) participant rate the overall quality of the motion in terms of naturalness (from 1 = “Very unnatural” to 5 = “Very natural”), motion smoothness (from 1 = “Very smooth” to 5 = “Very natural”), and alignment with the input sentence (from 1 = “Not at all” to 5 = “Perfectly aligned”). Then, we scaled each to 0 and 1 and inverted them. The second asks the participants to compare the motions generated by our methods and baselines (*ours-7*, *MD-7*, *ours-1* and MotionDiffuse) using the choices (“A”, “B”, “Both look similar to me”). We observe that our method has a preference score of $\sim 86\%$, $\sim 77\%$ and $\sim 80\%$ in naturalness, smoothness, and alignment to text input, respectively, as seen in Fig. 7.

8. Datasets

The KIT-ML dataset [35] provides 3911 motion sequences and 6353 sequence-level natural language descriptions. HumanML3D [12] re-annotates the AMASS dataset [30] and the HumanAct12 dataset [11]. It provides 44970 annotations on 14616 motion sequences.

9. Evaluation Metrics.

We adhere to evaluation protocols from [5, 53, 54, 57], assessing methods with four metrics (R-Precision, Fréchet Inception Distance (FID), Multi-modal Distance and Multimodality), each repeated 20 times with a 95% confidence interval.

- R-Precision:** measures motion-to-text retrieval accuracy by randomly selecting 31 mismatched text prompts and reporting top-k accuracies based on embeddings.
- Fréchet Inception Distance (FID):** evaluates realism and diversity of motions by comparing distributions of embeddings from generated and ground-truth data via a pretrained motion encoder.
- Multi-modal Distance:** uses a pretrained model to embed motions and calculates Euclidean distance between text and motion features.
- Multimodality:** assesses the diversity of motions from a single text by measuring joint position differences across 32 generated sequences.

10. Normalizing Flows

We use a real-valued non-volume preserving (Real-NVP) [7] as a probabilistic transformation, as depicted in the following equation:

$$[\sigma_\phi, \mu_\phi] = f_\phi(x_0^{i-1}, \varphi(u^{(j)}))$$

$$x_0^i = x_0^{i-1} \odot \sigma_\phi(x_0^{i-1}, \varphi(u^{(j)})) + \mu_\phi(x_0^{i-1}, \varphi(u^{(j)})), \quad (14)$$

where \odot is element-wise multiplication, and both σ_ϕ and μ_ϕ are deep feed-forward networks. During training, we inflate the input to the flow with a Gaussian noise with a small standard deviation for more robustness, as in Horvat et al. [22].

$$\tilde{x}_0^{i-1} = x_0^{i-1} + \epsilon_i \text{ where } \epsilon_i \sim \mathcal{N}(0, \sigma_{inf} I)$$

$$[\sigma_\phi, \mu_\phi] = f_\phi(\tilde{x}_0^{i-1}, \varphi(u^{(j)}))$$

$$x_0^i = x_0^{i-1} \odot \sigma_\phi(\tilde{x}_0^{i-1}, \varphi(u^{(j)})) + \mu_\phi(\tilde{x}_0^{i-1}, \varphi(u^{(j)})) \quad (15)$$

10.1. Numerical instability

While we attempted to adapt normalizing flows for temporal modelling by augmenting them with an LSTM, they still suffer from numerical instability, particularly during multi-step inverse flow computations. The primary source of this instability is the σ_ϕ function within the mapping,

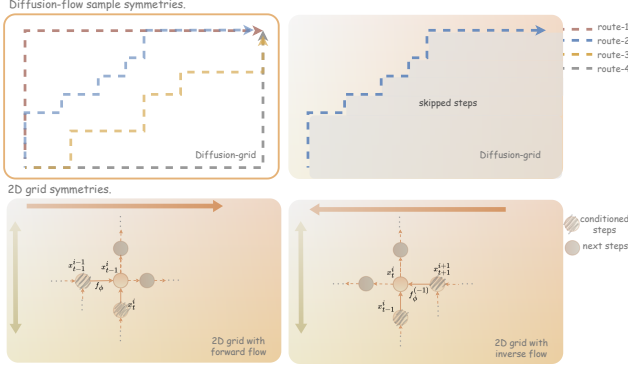


Figure 8. **Diffusion-flow symmetries.** By design, we can arrive at *diffusion-flow* samples following different routes. Some routes are more efficient than others as they allow for skipping diffusion sampling steps, but all are mathematically equivalent. **2D grid symmetries.** Normalizing flows properties gives us two grids (*forward-flow* and *inverse-flow*). Both are mathematically equivalent, but the *forward-flow* is more numerically stable.

where large values can cause an overflow of the inverse mapping $f_{\phi}^{(-i)}$, resulting in a NaN in the loss function.

We mitigated this by clamping the values to an acceptable range using a HardTanh function with limits of -0.1 and 0.1 . While this successfully resolved the instability in the loss, it did not address the issue of very long recurrence. We identify this as a limitation of our current method, and a more comprehensive analysis of this long-recurrence behaviour will be addressed in future work.

11. Notes on recurrent formulation properties

The design of our 2D grid exhibits inherent symmetries, which can be exploited to skip diffusion sampling steps, leading to more efficient inference. While this primarily benefits inference, a different configuration allows for efficient training, albeit with a trade-off in flexibility during the inference phase. This section will detail these properties and their implications for computational efficiency.

Diffusion-flow sample symmetries. By design, we can arrive at diffusion-flow samples through multiple mathematically equivalent sampling paths (see Fig. 8). Empirically, however, these paths yield varying sample quality and computational efficiency. Specifically, paths that rely on the normalizing flow for temporal sampling produce lower quality, as the flow has less capacity than the denoiser and is not as well-suited for temporal modelling. In terms of efficiency, paths that require fewer diffusion steps are more computationally efficient, particularly with larger sequence lengths, as the denoising process is the most expensive operation. This design, therefore, allows for an explicit trade-off between computational efficiency and sample quality.

2D grid symmetries. Since normalizing flows are invertible transformations, they allow for two distinct grid formulations for conditioning the reverse process: one with a forward flow and one with an inverse flow. We can thus condition the reverse process on either x_{t-1}^{i+1} or x_{t-1}^{i-1} . While both options are mathematically equivalent, conditioning on x_{t-1}^{i-1} is more numerically stable as it avoids computing an additional flow inverse transformation. We adopted this latter approach to parameterize our reverse flow and the associated loss function, as will be described in the next section.

12. RDM sampling

Unlike previous methods [5, 15, 53, 54], our approach does not require sampling Gaussian noise for the full sequence. Instead, we leverage the flow model to skip diffusion steps by sampling in a “staircase” through our 2D grid. This significantly enhances the computational efficiency and throughput when dealing with temporal data (see Algorithm 1).

The point at which we initiate this staircase sampling presents a unique trade-off between computational complexity and sampling quality. One extreme, which we term “disentangled sampling”, involves generating the first segment with *diffusion-only* and then rolling out the rest using only the normalizing flow. This offers the lowest computational complexity but results in the lowest sample quality, as it effectively disentangles the diffusion and temporal axis. The other extreme is to initiate the staircase from the beginning with our *diffusion-flow* approach. This path yields the highest computational complexity but also produces better sample quality. A comparison of these strategies is detailed in Tab. 4 and 5.

12.1. Beyond horizon inference complexity

To better understand the impact of sampling steps and model configuration on inference beyond the training horizon (196 frames), we compare three different RDM configurations (4, 7, and 14 segments) with varying DDIM sampling steps against CLoSD [46], in Fig. 10 and 9. RDM consistently proves more efficient than CLoSD [46] (shown on the left) and offers a significant speed advantage over CLoSD [46] (shown on the right). However, this speed advantage depends on the segment configuration and sequence length, with RDM-4 being the most efficient, followed by RDM-7 and RDM-14, which is the least efficient.

The computational complexity of all configurations RDM-4/7/14 rises with an increasing number of segments, with RDM-14 experiencing a nonlinear growth (DDIM-100, see Fig. 10). However, in Fig. 9 (DDIM-10), we see an increase, but around 280 it stabilises and maintains a steady speed. This is because we begin sampling only with the normalising flow (“disentangled sampling”) for the remaining frames. Note that we start staircase sampling at the

denoising step equal to the number of segments, and if it is not specified as in DDIM-10, we commence at the first step. Based on the rate of increase, if we extrapolate further and generate longer sequences without skipping steps, RDM will eventually reach CLoSD time complexity.

Algorithm 1 Sampling

```

1:  $x_T^0 \sim \mathcal{N}(0, I)$ 
2:  $\mathcal{S}_{out} := [x_T^0, f_\phi(x_T^0)]$ 
3: for  $t = T, \dots, 1$  do
4:    $\mathcal{S} = \mathcal{S}_{out}$ 
5:   for  $j = 0, \dots, i + 1$  do
6:      $z \sim \mathcal{N}(0, I)$  if  $t > 1$  else  $z = \mathbf{0}$ 
7:      $x_t^j = \mathcal{S}[j]$ 
8:      $x_{t-1}^{j-1} = \mathcal{S}_{out}[j - 1]$  if  $j > 0$  else  $x_{t-1}^{j-1} = \mathbf{0}$ 
9:      $x_t^0 = f_\phi^{(-j)}(\mathcal{S}[j])$ 
10:     $\epsilon_\theta^0 = f_\phi^{(-j)}(\epsilon_\theta(x_t^j, x_{t-1}^{j-1}, t, j))$ 
11:     $x_{t-1}^0 = \frac{1}{\sqrt{\alpha_t}}(x_t^0 - \frac{1-\alpha_t}{\sqrt{1-\alpha_t}}\epsilon_\theta^0) + \sigma_t z$ 
12:     $x_{t-1}^j = f_\phi^{(j)}(x_{t-1}^0)$ 
13:     $\mathcal{S}_{out}.append(x_{t-1}^j)$ 
14:  end for
15:  return  $\mathcal{S}_{out}$ 
16: end for
17: return  $\mathcal{S}_{out}$ 

```

13. Rollout diffusion baselines

To maintain flexibility and facilitate fair comparisons, we chose to denoise in pose space, similar to MotionDiffuse [54]. This decision was driven by the inherent limitations of latent diffusion methods, which require training a different VAE for each configuration of the number of segments, thereby complicating our ability to experiment with different recurrence lengths.

While our recurrent diffusion framework is agnostic to the choice of denoiser, we adopted the denoiser backbone from MotionDiffuse [54]. We chose this for its excellent performance and its widespread use in other baselines [15, 41, 55], which establishes MotionDiffuse as our closest comparison point.

For a rigorous evaluation, we trained custom MotionDiffuse [54] baselines to handle variable sequence horizons, mirroring our training setup. This baseline, which takes corrupted motion segments and predicts the next clean segments, was trained in two settings: one with 4 segments (MD-4) and another with 7 segments (MD-7). These MD-x baselines effectively represent RDM’s architecture without recurrent connections, with diffusion applied to each segment independently. This effectively makes MD-x serve as an ablation of RDM’s recurrent connection.

14. Rollout datasets baselines

The standard train-test split in KIT-ML dataset [35] and HumanML3D [12] followed by previous methods [5, 53, 54, 57], we constructed a new split named *rolout-split* consisting of sequences in train or test sets with sequences having total frames larger than the training horizon, which were previously trimmed by other methods and use them to evaluate rollout performance (see Appendix 14).

Algorithm 2 diffusion_update_step

```

1: repeat
2:    $x_0 \sim q(\mathcal{X})$  // sample sequence
3:    $x_0^0 := select\_at([x^i]_{i=0}^L, 0)$  // select 1st segment
4:    $t \sim Uniform(1, \dots, T)$ 
5:    $i \sim Uniform(0, \dots, L)$ 
6:    $\epsilon_\theta^0 \sim \mathcal{N}(\mathbf{0}, \mathbf{I})$ 
7:    $x_t^i = f_\phi^{(i)}(\sqrt{\alpha_t}x_0^0 + \sqrt{1-\alpha_t}\epsilon_\theta^0)$ 
8:    $x_{t-1}^{i-1} = f_\phi^{(i-1)}(\sqrt{\alpha_{t-1}}x_0^0 + \sqrt{1-\alpha_{t-1}}\epsilon_\theta^0)$ 
9:   Take gradient step on
10:     $\nabla_\theta \|x_0^i - f_\theta(x_t^i, x_{t-1}^{i-1}, t, i)\|^2$ 
11: until end of epoch

```

15. Implementation details

Training settings. We train RDM using MoMo-Adam optimizer [40] with a learned rate $1e^{-4}$ for the flow and $2e^{-4}$ learning rate for the diffusion denoiser model, with a batch size 512. Our full training takes ~ 4.5 days on 2 H100 Nvidia GPUs. We train the full model for 50 epochs in total, and we artificially increased the data length by a factor of 25 for each GPU used. We train the flow and denoiser together to minimize the reconstruction loss (see Algorithm 2).

For inference-time comparison and computational efficiency, we ran all evaluations at a batch size of 128 and a sequence length of 196 20 times, reporting the mean inference time and standard deviation. For the FLOPs, we use the *calgflops* Python package to calculate the flops on a batch size of 1 with 196 sequence length. We ran both experiments on a single NVIDIA H100 GPU.

Architectures. We use 4/7 segments for a maximum sequence length of 196, yielding a segment length of 49/28 frames. For normalizing flow, we used a 1 layer LSTM with 256 hidden dimensions, and for the invertible transformation, we used 256 feature dimensions and 6 transformation blocks. For the diffusion denoiser, we utilise a similar temporal transformer-based architecture to that of MotionDiffuse [54]. We used 8 transfer layers with 512 latent dimensions and with 8 heads. As for the text conditioning, we used a pre-trained CLIP ViT-B/32 model CLIP [36] to encode text and then added four more transformer encoder

Method	R-Precision (\uparrow)			FID (\downarrow)	MultiModal Dist (\downarrow)	MultiModality (\uparrow)
	Top 1	Top 2	Top 3			
Real motions	0.5138	0.6957	0.7937	0.002 \pm .000	2.974 \pm .008	-
Disentangle	0.3022 \pm .0091	0.4954 \pm .0084	0.6161 \pm .0063	6.2045 \pm .1114	4.4230 \pm .05	1.6361 \pm .1407
Entangle-996	0.405 \pm .002	0.593 \pm .003	0.702 \pm .002	0.402 \pm .018	3.651 \pm .008	1.199 \pm .04
Entangle-900	0.334 \pm .012	0.537 \pm .005	0.667 \pm .01	3.824 \pm .233	2.761 \pm .019	1.284 \pm .078
Entangle-800	0.335 \pm .005	0.539 \pm .006	0.674 \pm .002	3.648 \pm .221	3.821 \pm .06	1.241 \pm .115

Table 4. **Quantitative results on the KIT-ML [35] test set.** All methods use ground truth motion length. Evaluations were conducted 20 times with 95% CI reported. Rows are colour-coded as **best**, **second best**, and **third best**. RDM’s staircase sampling trade-off between computational complexity and sampling quality. We found that starting the sampling at segment length provides the best result compared to starting earlier (Entangle- x , where x indicates the staircase sampling start) or “disentangled”, where we sample the first segment with “diffusion-only” and roll out the rest with “flow-only”. We use RMD-7 for all experiments.

Method (RDM-7)	Total Inference Time (s) \downarrow		Parameters
	FLOPs (T) \downarrow		
	DDPM	DDPM	
	1000	1000	
Disentangle	11.10 \pm .59	2.31	$x \in \mathbb{R}^{49 \times 251}$
Entangle-997	11.7 \pm 2.02	2.32	$x \in \mathbb{R}^{49 \times 251}$
Entangle-900	13.37 \pm .31	4.06	$x \in \mathbb{R}^{49 \times 251}$
Entangle-800	18.02 \pm 4.14	5.5	$x \in \mathbb{R}^{49 \times 251}$

Table 5. **Inference time comparison.** All methods use ground truth motion length. Evaluations were conducted 20 times with 95% CI reported. Rows are colour-coded as **best**, **second best**, and **third best**. RDM’s staircase sampling trade-off between computational complexity and sampling quality. Although “disentangled sampling” (sampling the first segment with “diffusion-only” and the rest with “flow-only”) has the lowest cost, it yields the worst results compared to Entangle- x , which starts staircase sampling at point x .

layers. The latent dimension of the text encoder and the motion decoder are 256 and 512, respectively. As for the diffusion model, the number of diffusion steps is 1000, and the variances β_t are linearly from 0.0001 to 0.02.

To incorporate temporal conditioning, we used positional encoding with different frequencies for the diffusion frame number and different shallow MLPs to encode temporal and spatial steps into latent spaces. We follow the same conditioning method as in MotionDiffuse [54] and add the mapped latents of frame and time to the projected text embedding. Then apply cross-attention in the transformer to predict the denoiser, as in MotionDiffuse [54].

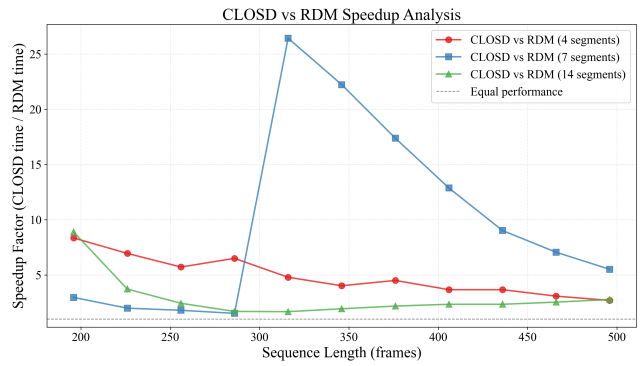
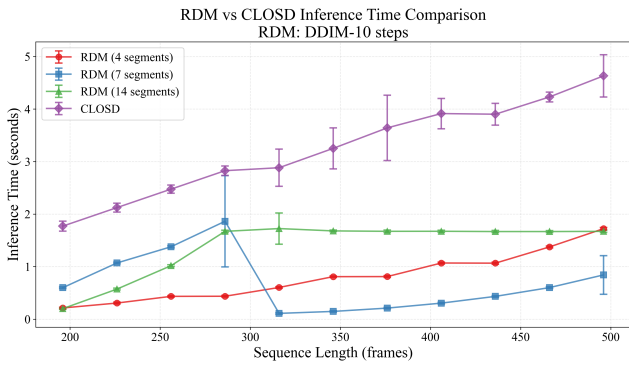


Figure 9. **Computational efficiency comparison between RDM and CLoSD (DIP) [46].** (left) Inference time versus sequence length for RDM with three segment numbers (4, 7, 14 segments, DDIM-10 steps) and CLoSD (DIP). Error bars represent ± 3 standard deviation. (right) Speedup analysis showing CLoSD (DIP) inference time divided by RDM inference time. RDM consistently outperforms CLoSD (DIP) by a significant margin across all sequence lengths, with higher speedups for shorter sequences. The speedup depends on the segment configuration: RDM-4 is more efficient than RDM-7, and RDM-14 is the least efficient.

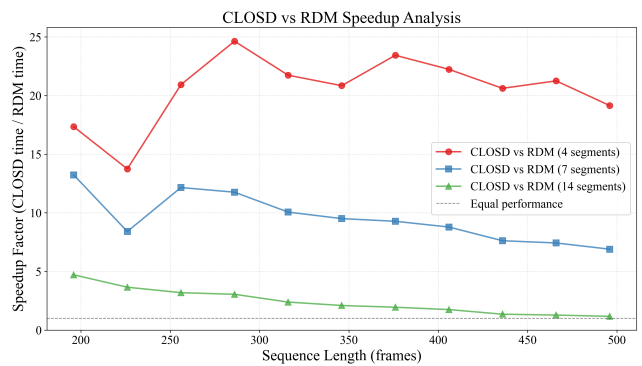
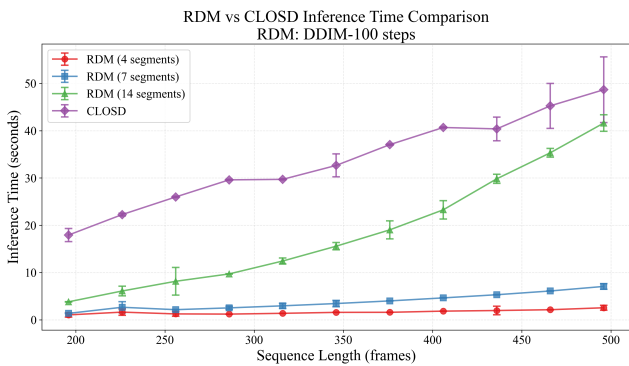


Figure 10. **Computational efficiency comparison between RDM and CLoSD (DIP) [46].** (left) Inference time versus sequence length for RDM with three segment numbers (4, 7, 14 segments, DDIM-100 steps) and CLoSD (DIP). Error bars represent ± 3 standard deviation. (right) Speedup analysis showing CLoSD (DIP) inference time divided by RDM inference time. RDM consistently outperforms CLoSD (DIP) by a significant margin across all sequence lengths, with higher speedups for shorter sequences. The speedup depends on the segment configuration: RDM-4 is more efficient than RDM-7, and RDM-14 is the least efficient.

16. Loss derivation (proof)

We use the forward normalizing flow according to the 2D grid defined in the previous section 11. As discussed in the main text, our forward diffusion process across the grid is defined by the following equations:

$$q(x_{1:T}^i | x_0^i, x_T^{i-1}) = \prod_{t=1}^T q(x_t^i | x_{t-1}^i, x_t^{i-1}) \quad (16)$$

$$q(x_{1:T}^{1:L} | x_0^0, x_T^{0-1}) = \prod_{t=1}^T q(x_t^{1:L} | x_{t-1}^{1:L}) \quad (17)$$

$$q(x_{1:T}^{1:L} | x_0^0, x_T^{0-1}) = \prod_{i=1}^L \prod_{t=1}^T q(x_t^i | x_{t-1}^i, x_t^{i-1}) \quad (18)$$

As we are using a 2D grid with forward normalizing flow, then our reverse diffusion process is defined by the next equations:

$$p_\theta(x_{1:T}^i | x_0^i, x_T^{i-1}) = \prod_{t=1}^T p_\theta(x_{t-1}^i | x_t^i, x_t^{i-1}) \quad (19)$$

$$p_\theta(x_{0:T}^{0:L}) = p(x_T^{0:L}) \prod_{t=1}^T p_\theta(x_{t-1}^{0:L} | x_t^{0:L}) \quad (20)$$

$$p_\theta(x_{0:T}^{0:L}) = p(x_T^0) \prod_{i=1}^L \prod_{t=1}^T p_\theta(x_{t-1}^i | x_t^i, x_t^{i-1}) \quad (21)$$

$$(22)$$

Let us begin by equating our data log probability $\log(p_\theta(x_0^{0:L}))$ as follows:

$$\begin{aligned} -\log(p_\theta(x_0^{0:L})) &\leq -\log(p_\theta(x_0^{0:L})) + D_{kl}(q(x_{1:T}^{0:L} | x_0^{0:L}) \| p_\theta(x_{1:T}^{0:L} | x_0^{0:L})) \\ &= -\log(p_\theta(x_0^{0:L})) + \mathbb{E}_{x_{1:T}^{0:L} \sim q(x_{1:T}^{0:L} | x_0^{0:L})} \left[\log \frac{q(x_{1:T}^{0:L} | x_0^{0:L})}{p_\theta(x_{0:T}^{0:L}) / p_\theta(x_0^{0:L})} \right] \\ &= \mathbb{E}_q \left[\log \frac{q(x_{1:T}^{0:L} | x_0^{0:L})}{p_\theta(x_{0:T}^{0:L})} \right] \end{aligned}$$

Then let $\mathcal{L}_{VLB} = \mathbb{E}_{q(x_0^0:L)} \left[\log \frac{q(x_1^0:L|x_0^0:L)}{p_\theta(x_0^0:L)} \right] \geq -\mathbb{E}_{q(x_0^0:L)} p_\theta(x_0^0:L)$

$$\begin{aligned}
\mathcal{L}_{VLB} &= \mathbb{E}_q \left[\log \frac{q(x_1^0:L|x_0^0:L)}{p_\theta(x_0^0:L)} \right] \\
&= \mathbb{E}_q \left[\log \frac{\prod_{t=1}^T q(x_t^0:L|x_{t-1}^0:L)}{p_\theta(x_0^0:L) \prod_{t=1}^T p_\theta(x_{t-1}^0:L|x_t^0:L)} \right] \\
&= \mathbb{E}_q \left[-\log(p_\theta(x_0^0:L)) + \sum_{t=1}^T \log \frac{q(x_t^0:L|x_{t-1}^0:L)}{p_\theta(x_{t-1}^0:L|x_t^0:L)} \right] \\
&= \mathbb{E}_q \left[-\log(p_\theta(x_0^0:L)) + \sum_{t=2}^T \log \frac{q(x_t^0:L|x_{t-1}^0:L)}{p_\theta(x_{t-1}^0:L|x_t^0:L)} + \log \frac{q(x_1^0:L|x_0^0:L)}{p_\theta(x_0^0:L|x_1^0:L)} \right] \\
&= \mathbb{E}_q \left[-\log(p_\theta(x_0^0:L)) + \sum_{t=2}^T \log \left(\frac{q(x_{t-1}^0:L|x_t^0:L, x_0^0:L)}{p_\theta(x_{t-1}^0:L|x_t^0:L)} \cdot \frac{q(x_t^0:L|x_0^0:L)}{q(x_{t-1}^0:L|x_0^0:L)} \right) + \log \frac{q(x_1^0:L|x_0^0:L)}{p_\theta(x_0^0:L|x_1^0:L)} \right] \text{ (Bayes's rule)} \\
&= \mathbb{E}_q \left[-\log(p_\theta(x_0^0:L)) + \sum_{t=2}^T \log \frac{q(x_{t-1}^0:L|x_t^0:L, x_0^0:L)}{p_\theta(x_{t-1}^0:L|x_t^0:L)} + \sum_{t=2}^T \log \frac{q(x_t^0:L|x_0^0:L)}{q(x_{t-1}^0:L|x_0^0:L)} + \log \frac{q(x_1^0:L|x_0^0:L)}{p_\theta(x_0^0:L|x_1^0:L)} \right] \\
&= \mathbb{E}_q \left[-\log(p_\theta(x_0^0:L)) + \sum_{t=2}^T \log \frac{q(x_{t-1}^0:L|x_t^0:L, x_0^0:L)}{p_\theta(x_{t-1}^0:L|x_t^0:L)} + \log \frac{q(x_T^0:L|x_0^0:L)}{q(x_1^0:L|x_0^0:L)} + \log \frac{q(x_1^0:L|x_0^0:L)}{p_\theta(x_0^0:L|x_1^0:L)} \right] \\
&\quad \text{(Intermediate terms cancels)} \\
&= \mathbb{E}_q \left[\log \frac{q(x_T^0:L|x_0^0:L)}{p_\theta(x_T^0:L)} + \sum_{t=2}^T \log \frac{q(x_{t-1}^0:L|x_t^0:L, x_0^0:L)}{p_\theta(x_{t-1}^0:L|x_t^0:L)} - \log(p_\theta(x_0^0:L|x_1^0:L)) \right] \text{ (Rearranging logs)} \\
&= \mathbb{E}_q \left[\underbrace{D_{kl}(q(x_T^0:L|x_0^0:L)||p_\theta(x_T^0:L))}_{\mathcal{L}_T^{0:1}} + \sum_{t=2}^T \underbrace{D_{kl}(q(x_{t-1}^0:L|x_t^0:L, x_0^0:L)||p_\theta(x_{t-1}^0:L|x_t^0:L))}_{\mathcal{L}_{t-1}^{0:L}} + \underbrace{\mathbb{E}_q[-\log(p_\theta(x_0^0:L|x_1^0:L))]}_{\mathcal{L}_0^{0:L}} \right]
\end{aligned}$$

Let us label each term in the lower bound separately and further expand them:

$$\begin{aligned}
\mathcal{L}_T^{0:1} &= D_{kl}(q(x_T^0:L|x_0^0:L)||p_\theta(x_T^0:L)) = \mathbb{E}_q \left[\log \left(\frac{q(x_T^0|x_0^0) \prod_{i=1}^L q(x_T^i|x_0^i, x_T^{i-1})}{p_\theta(x_T^0) \prod_{i=1}^L p_\theta(x_T^i|x_T^{i-1})} \right) \right] \\
&= \mathbb{E}_q \left[\log \frac{q(x_T^0|x_0^0)}{p_\theta(x_T^0)} + \sum_{i=1}^L \log \frac{q(x_T^i|x_0^i, x_T^{i-1})}{p_\theta(x_T^i|x_T^{i-1})} \right] \\
&= \underbrace{D_{kl}(q(x_T^0|x_0^0)||p_\theta(x_T^0))}_{\mathcal{L}_T^0} + \sum_{i=1}^L \underbrace{D_{kl}(q(x_T^i|x_0^i, x_T^{i-1})||p_\theta(x_T^i|x_T^{i-1}))}_{\mathcal{L}_T^i}
\end{aligned}$$

$$\begin{aligned}
\mathcal{L}_0^{0:L} &= -\log(p_\theta(x_0^0:L|x_1^0:L)) = -\log(p_\theta(x_0^0|x_1^0) - \log(\prod_{i=1}^L p_\theta(x_0^i|x_0^{i-1}, x_1^i))) \\
&= \underbrace{-\log(p_\theta(x_0^0|x_1^0))}_{\mathcal{L}_0^0} + \sum_{i=1}^L \underbrace{-\log(p_\theta(x_0^i|x_0^{i-1}, x_1^i))}_{\mathcal{L}_0^i}
\end{aligned}$$

$$\begin{aligned}
\mathcal{L}_{t-1}^{0:L} &= D_{kl}(q(x_{t-1}^{0:L}|x_t^{0:L}, x_0^{0:L})\|p_\theta(x_{t-1}^{0:L}|x_t^{0:L})) = \log \frac{q(x_{t-1}^{0:L}|x_t^{0:L}, x_0^{0:L})}{p_\theta(x_{t-1}^{0:L}|x_t^{0:L})} \\
&= \log \left(\frac{q(x_{t-1}^0|x_t^0, x_0^0) \prod_{i=1}^L q(x_{t-1}^i|x_t^i, x_{t-1}^{i-1}, x_0^i)}{p_\theta(x_{t-1}^0|x_t^0) \prod_{i=1}^L p_\theta(x_{t-1}^i|x_t^i, x_{t-1}^{i-1})} \right) = \mathbb{E}_q \left[\log \frac{q(x_{t-1}^0|x_t^0, x_0^0)}{p_\theta(x_{t-1}^0|x_t^0)} + \sum_{i=1}^L \log \frac{q(x_{t-1}^i|x_t^i, x_{t-1}^{i-1}, x_0^i)}{p_\theta(x_{t-1}^i|x_t^i, x_{t-1}^{i-1})} \right] \\
&= \underbrace{D_{kl}(q(x_{t-1}^0|x_t^0, x_0^0)\|p_\theta(x_{t-1}^0|x_t^0))}_{\mathcal{L}_{t-1}^0} + \sum_{i=1}^L \underbrace{D_{kl}(q(x_{t-1}^i|x_t^i, x_{t-1}^{i-1}, x_0^i)\|p_\theta(x_{t-1}^i|x_t^i, x_{t-1}^{i-1}))}_{\mathcal{L}_{t-1}^i}
\end{aligned}$$

Our final variational lower bound \mathcal{L}_{VLB} takes the form:

$$\begin{aligned}
\mathcal{L}_{VLB} &= \sum_{i=0}^L \sum_{t=0}^T \mathcal{L}_t^i = \sum_{i=0}^L [\mathcal{L}_T^i + \sum_{i=2}^T \mathcal{L}_{t-1}^i + \mathcal{L}_0^i] \\
&= D_{kl}(q(x_T^0|x_0^0)\|p_\theta(x_T^0)) + \sum_{t=2}^T D_{kl}(q(x_{t-1}^0|x_t^0, x_0^0)\|p_\theta(x_{t-1}^0|x_t^0)) - \log(p_\theta(x_0^0|x_1^0)) \\
&\quad + \sum_{i=1}^L [D_{kl}(q(x_T^i|x_0^i, x_T^{i-1})\|p_\theta(x_T^i|x_T^{i-1})) + \sum_{t=2}^T D_{kl}(q(x_{t-1}^i|x_t^i, x_{t-1}^{i-1}, x_0^i)\|p_\theta(x_{t-1}^i|x_t^i, x_{t-1}^{i-1})) \\
&\quad - \log(p_\theta(x_0^i|x_0^{i-1}, x_1^i))]
\end{aligned} \tag{23}$$

16.1. Parameterization of training Loss.

Each \mathcal{L}_T^i is constant with respect to the diffusion encoder and can be ignored because q has no learnable parameters and x_T^0 is a Gaussian noise, while x_T^i are defined with the flow which is only updated with the x_0 . Every KL term in \mathcal{L}^0 except \mathcal{L}_0^0 compares two Gaussians and is computed in a closed form. The remaining are the KL terms in \mathcal{L}^1 : except \mathcal{L}_0^1 . Each compares two unknown distributions and is defined using the normalizing flow.

$$\begin{aligned}
\mathcal{L}_{t-1}^i &= D_{KL}(q_\phi(x_{t-1}^i|x_t^i, x_{t-1}^{i-1}, x_0^i)\|p_\theta(x_{t-1}^i|x_t^i, x_{t-1}^{i-1})) \\
\mathcal{L}_{t-1}^i &= \sum_{x_{t-1}^i} q_\phi^i(x_{t-1}^i|x_t^i, x_{t-1}^{i-1}, x_0^i) \left[\log \frac{q_\phi(x_{t-1}^i|x_0^i, x_0^0)}{p_\theta(x_{t-1}^i|x_t^i, x_{t-1}^{i-1})} \right]
\end{aligned}$$

The case of linear flow. As we restrict our flow to a linear transformation, the resulting distributions remain Gaussian. All KL terms in \mathcal{L}^1 : are computed in closed form, with mean shifted and standard deviation scaled according to the normalizing flow. Depending on the parametrization, we arrive at the same loss as Ho et al. [18] with different weight terms.

$$\mathcal{L}_{t-1}^i = D_{KL}(\mathcal{N}(x_{t-1}^i; \mu(x_t^i, x_{t-1}^{i-1}, x_0^i), \Sigma_t) \| \mathcal{N}(x_{t-1}^i; \mu_\theta(x_t^i, x_{t-1}^{i-1}, t, i), \Sigma_\theta)) \tag{24}$$

$$\mathcal{L}_{t-1}^i = \mathbb{E}_q [\tilde{w}(t) \|x_0^i - f_\theta(x_t^i, x_{t-1}^{i-1}, t, i)\|^2] \quad (\text{Same as diffusion loss}) \tag{25}$$

Where $\tilde{w}(t)$ represents the signal-to-noise ratio, accounting for the flow transformation as well, and can take different forms depending on the chosen parameterization. Here we show the case of the parameterization in Ho et al. [18], but other parametrizations cases are easily obtained:

$$\tilde{w}(t) = \frac{\beta_t^2}{2\sigma_t^2 \alpha_t (1 - \bar{\alpha})} \left| \det \frac{\partial f_\phi}{\partial x_0^i} \right|^{-1}$$

The generic case of non-linear flow. Since we employ a generic nonlinear flow, each KL term in \mathcal{L}^1 : except \mathcal{L}_0^1 compares two unknown distributions defined via a normalizing flow. Learning the posterior of these distributions often requires methods like Markov Chain Monte Carlo (MCMC) [32, 48]; however, MCMC methods have slow convergence, making the learning infeasible with 1000 diffusion steps. This raises a key question: how can we efficiently learn the reverse process? To address this, we leverage the properties of normalizing flow to derive a closed-form solution for these KL terms as follows.

First, we employ the inverse flow to map the samples x_t^i to the *diffusion-only* frame x_t^0 . In the diffusion-only case, everything is Gaussian, allowing us to compute the KL in closed form. Then, we transfer the distribution back to the temporal step i via the forward flow. This results in a KL between two normal distributions with additional weighting terms based on the inverse determinant of the derivative of the normalizing flow transformation, as shown in the next equation:

$$\begin{aligned} \log(q_\phi(x_{t-1}^i|x_t^i, x_{t-1}^{i-1}, x_0^i)) &= \log \mathcal{N}(x_{t-1}^0) - \sum_{j=1}^i \log \left| \det \frac{\partial f_\phi}{\partial x_0^0} \right| \quad (\text{Flow properties}) \\ \log(p_\theta(x_{t-1}^i|x_t^i, x_{t-1}^{j-1})) &= \log \mathcal{N}(f^{-i}(x_{t-1}^i)) - \sum_{j=1}^i \log \left| \det \frac{\partial f_\phi}{\partial x_0^i} \right| \quad (\text{Flow properties}) \\ \mathcal{L}_{t-1}^i &= \sum_x q_\phi(x_{t-1}^0|x_t^0, x_0^0) \log \frac{\mathcal{N}(x_{t-1}^0; \mu(x_{t-2}^0, x_0^0), \beta_t)}{\mathcal{N}(f^{-i}(x_{t-1}^i); \mu_\theta(x_t^i, x_{t-1}^{i-1}, t, i), \Sigma_\theta)} \left| \det \frac{\partial f_\phi}{\partial x_0^i} \right|^{-1} \\ &\quad (\text{Flow properties}) \end{aligned}$$

The KL between two Gaussians is computed in closed form, and following a similar parametrization to Ho et al. [18], the loss is further reduced to the difference between means, as depicted in the following equation:

$$\mathcal{L}_t^i = \mathbb{E}_{q^0}[w(t) \left| \det \frac{\partial f_\phi}{\partial x_0^i} \right|^{-1} \|\mu(x_t^i, x_{t-1}^{i-1}, x_0^i) - \mu_\theta(x_t^i, x_{t-1}^{i-1}, t, i), t, i\|^2] \quad (\text{Same as diffusion loss}) \quad (26)$$

The question remains, how to get the means of the distribution at the *diffusion-only*. As the forward process follows a Markovian chain, the mean is simply the previous noised sampled segment x_{t-1}^0 . We choose to predict the clean segment, and we get the predicted mean following the grid (using the inverse flow and the forward diffusion) as follows:

$$\mu(x_t^i, x_{t-1}^{i-1}, x_0^i) = \sqrt{\bar{\alpha}_t} x_0^0 + \sqrt{1 - \bar{\alpha}_t} \epsilon \quad (27)$$

$$\mu_\theta(x_t^i, x_{t-1}^{i-1}, t, i) = \sqrt{\bar{\alpha}_t} \hat{x}_0^0 + \sqrt{1 - \bar{\alpha}_t} \epsilon \quad (28)$$

$$\mathcal{L}_{t-1}^i = \bar{\alpha}_t \|x_0^0 - \hat{x}_0^0\|_2^2 \quad (29)$$

$$\mathcal{L}_{t-1}^i = \bar{\alpha}_t \|f_\phi^{(-i)}(x_0^i) - f_\phi^{(-i)}(\hat{x}_0^i)\|_2^2 \quad (30)$$

We found that the previous loss Eq. (30) is unstable and difficult to optimize because it relies on the numerical stability of the inverse flow and assumes a perfect flow model. This causes the performance of the diffusion model depend on the flow's effectiveness. Therefore, we decided to optimize the subsequent loss instead. As the flow is smooth mapping, we can employ the Taylor expansion series around 0, which leads us to the following equation:

$$\mathcal{L}_{t-1}^i = \mathbb{E}_{q^0}[w(t) \left| \det \frac{\partial f_\phi}{\partial x_0^i} \right|^{-1} \|x_0^i - f_\theta(x_t^i, f_{t-1}^{i-1}, t, i)\|^2] \quad (\text{Same as diffusion loss}) \quad (31)$$